Start and stop of an avalanche in a granular medium subjected to an inner water flow

P. Philippe and T. Richard
Cemagref, 3275 route de Cézanne, CS40061, 13182 Aix-en-Provence Cedex 5, France
(Received 27 November 2007; revised manuscript received 8 February 2008; published 16 April 2008)

We report experimental results on the maximum angle of stability, i.e., the so-called *avalanche angle*, of a granular medium subjected to an inner water flow controlled by a constant pressure drop. A unique avalanche threshold is derived by two alternative theoretical developments, namely a continuum and a discrete approach, and is successfully confronted to many measurements in a large experimental range. A qualitative analysis of the instability triggering reveals different dynamical behaviors depending on whether the water flow is downward or upward in the granular layer, namely *stabilizing* versus *destabilizing* regime. Contrary to the purely hydrostatic situation, the free surface following an avalanche departs from a linear shape because the dynamical pressure gradient is no longer constant in the medium. A simple model is proposed that can satisfactorily predict the postavalanche height profile as well as its subsequent evolution for higher inclinations.

DOI: 10.1103/PhysRevE.77.041306 PACS number(s): 45.70.Ht, 47.55.Lm, 47.56.+r

I. INTRODUCTION

Gravitational stability of a soil is a major concern for both civil engineering structures and for natural hazards since slope failures can trigger large surface avalanches, massive landslides [1], or potentially devastating debris flows [2]. Such events occur in subaerial as well as in subaqueous environments and, for instance, landslides are frequently observed on the seafloor, even on very slight inclines [1]. For fully saturated soils, groundwater flow affects soil stability and, according to streamlines orientation versus gravity, can possibly lead to fluidization [3] or to slope failure. Downstream face sliding on an earth dam, submarine landslide, or quicksand are some related examples of gravitational instabilities induced by groundwater flows.

The present work deals with the situation of an immersed granular medium subjected to an inner water flow, either in an upward or downward direction in respect to its free surface normal. The main question is to understand how the whole drag force exerted on the grains by the flow will enhance or reduce the overall stability of the medium. In the specific case of granular media, the stability threshold is simply determined by the maximum stable slope inclination also called *avalanche angle*. The aim of this study is to focus both theoretically and experimentally on the influence of a steady inner water flow on the avalanche angle of a granular layer and on its subsequent dynamics. To tackle this issue, granular physics, soil slope stability, and fluid dynamics in porous media must be brought together.

To our knowledge, only a few studies have investigated experimentally the effect of an inner fluid flow on the stability angle of a granular medium. In the case of a water flow, van Rhee and Bezuijen have proposed two distinct failure modes, namely a continuum mode and a single-particle mode, depending on whether the flow is outward or inward [4]. Some experimental data approximately verify the theoretical relations but without any explanation for this obvious influence of the flow direction on the adequate failure criterion. In a more recent study and for a similar situation, Lu *et al.* have solely considered a stability criterion based on a local particle equilibrium [5]. But their theoretical prediction, different and to our mind much more reliable than the previous one, must be modified by an arbitrary shift to roughly agree with several experimental data, obtained only in a small range of angles. In the case of a gas flow within the medium, Eames and Gilbertson have carried out an exhaustive study of aerated granular flows where different expressions have been proposed for the repose angle of a granular material poured on a horizontal surface [6]. These expressions depend on whether a continuum or a single particle approach is preferred, and also on whether a low or a high Reynolds number description is used for the drag force exerted on a single particle by the gas flow. According to their experimental results, distinct expressions must be selected for a conical granular pile and for a quasi-bidimensional pile for which the influence of the lateral walls cannot be neglected.

The paper is organized as follows. After a description of the setup in Sec. II, both continuum and discrete theories are proposed in Sec. III and produce the same theoretical prediction for the avalanche angle of a granular layer subjected to an inner water flow. In Sec. IV, this prediction is successfully confronted to a large set of experimental data and the different regimes of the instability dynamics (*destabilizing* vs *stabilizing* regime) are qualitatively described. The profile of the static-free surface following an avalanche, which departs significantly from a linear slope in the stabilizing regime, is also studied experimentally and theoretically. Finally, Sec. V summarizes the findings and draws some plans for further research.

II. EXPERIMENTAL SETUP

A diagram of the experimental setup is presented in Fig. 1. It consists of a granular sample poured in water inside a partially transparent rectangular cell with inner dimensions of $20 \times 5 \times 40$ cm (length $\times$ width $\times$ height). The top and the bottom of the cell are connected to two different water reservoirs so as to establish a controlled downward or upward flow in the granular medium. The flow is homogeneously distributed by two layers of large glass beads (1 cm diameter) positioned at the bottom and at the top of the cell. The

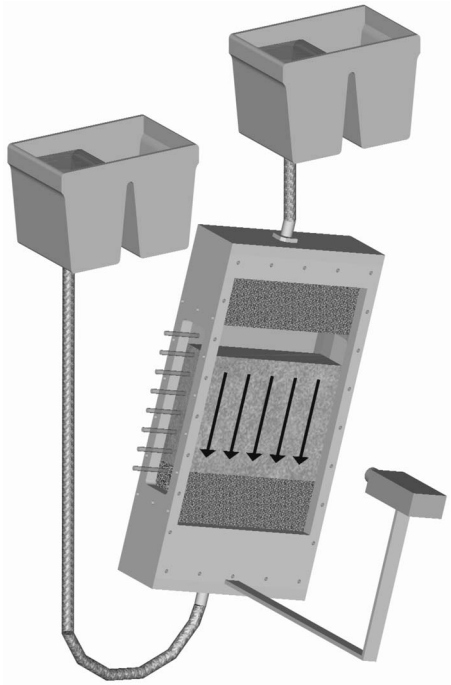

FIG. 1. Diagram of the experimental setup constituted of two constant level tanks and of a rotating cell with a set of eight pore pressure ports (on the left lateral wall), two flow distributors, and a camera. The black arrows depict the seepage streamlines (downward in the present configuration) parallel to the lateral walls.

granular sample lies on a fine grid placed over the lower distributor. A set of eight pore pressure ports has been fixed in the left lateral wall and a camera is used to record the movement of the grains at the front wall. The whole system (cell+camera) is rotated at small speed by a direct current motor. Nearly all the experiments presented here were performed with different samples of spherical glass beads, having mean diameters d ranging from 0.3 to 3 mm. A few sets of experiments were also carried out with a natural sand (0.4–0.8 mm). Figure 2 presents a schematic diagram of the cell containing a granular layer of height H.

Inside the granular bed, the total water pressure gradient reads

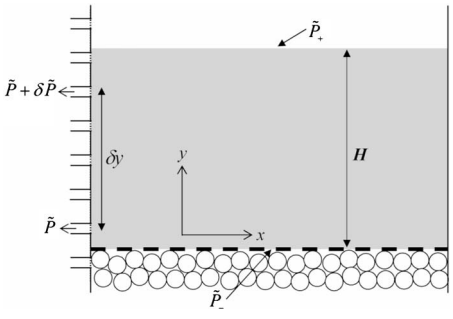

FIG. 2. Schematic diagram of the cell with the eight ports pressure in the left lateral wall, the upper and lower nonhydrostatic pressure $\tilde{P}_+$ and $\tilde{P}_-$, and the coordinate axes in the cell frame. $\delta\tilde{P}$ denotes the pressure drop between two ports pressure separated by a distance δy.

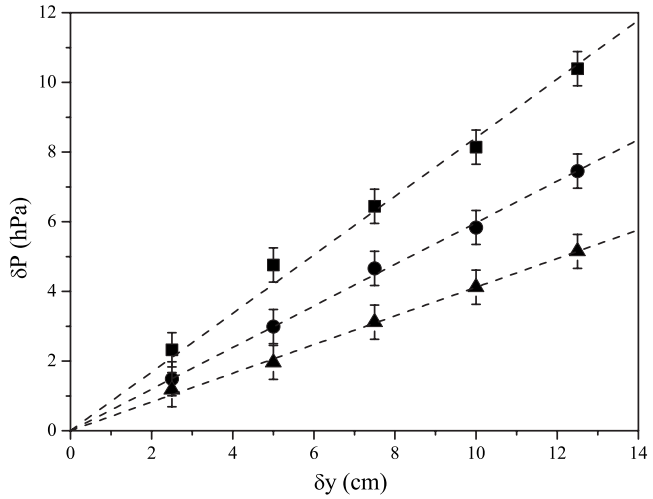

FIG. 3. Vertical profiles of the nonhydrostatic water pressure, $\delta\tilde{P}$ versus δy (defined in Fig. 2), measured inside a granular sample ($H=15.6$ cm and $\Phi=0.600$) constituted of glass beads ($d=1.0\pm0.1$ mm) and with three different water velocities: $v=0.97$ cm s^{-1} and $i=0.86$ (■), $v=0.65$ cm s^{-1}, and $i=0.61$ (●), $v=0.42$ cm s^{-1}, and $i=0.42$ (▲).

$$\text{grad } P = \rho_w \underline{g} + \text{grad } \tilde{P}, \tag{1}$$

where P and $\tilde{P}$ are, respectively, the total pressure and the nonhydrostatic pressure, ρ_w the water density ($\rho_w \simeq 10^3$ kg m^{-3}), and $\underline{g}$ the gravitational acceleration ($\|\underline{g}\|=9.81$ m s^{-2}). In this expression, the first term denotes the hydrostatic pressure gradient, corresponding to buoyancy, and the second one is the pressure drop associated to the viscous loss induced by the water flow through the granular medium. Alternatively, we can also introduce a nondimensional form of the nonhydrostatic pressure gradient which is $\underline{i}$, usually called *hydraulic gradient* by hydrologists, and defined by

$$\rho_w g \underline{i} = \text{grad } \tilde{P} \tag{2}$$

The setup imposes that $\tilde{P}$ is constant at the top and at the bottom boundary of the granular bed [7]. Let denote $\tilde{P}_+$ and $\tilde{P}_-$ the corresponding values, respectively, at the upper and at the lower surface. Assuming that the medium is homogeneous and isotropic, the flow streamlines are parallel to the lateral walls (i.e., perpendicular to the free surface), as depicted by the arrows on Fig. 1. In the cell frame, with the coordinate axes defined in Fig. 2, the nonhydrostatic gradient pressure reads simply $\text{grad } \tilde{P} = -(\frac{\Delta\tilde{P}}{H})\underline{y}$ with $\Delta\tilde{P}=\tilde{P}_- - \tilde{P}_+$ and where $\underline{y}$ is the unit vector along the y axis. In a nondimensional form, the corresponding hydraulic gradient is $\underline{i}=-i\underline{y} = -(\frac{\Delta\tilde{P}}{\rho_w g H})\underline{y}$. To check the validity of the homogeneity assumption, some pressure profiles were measured inside a glass beads sample with a differential pressure sensor by means of the lateral pore pressure ports. As can be seen in Fig. 3, these pressure profiles are actually almost linear and the granular layer is consequently reasonably homogeneous.

The protocol used to obtain reproducible samples is described later in Sec. IV A.

Two distinct water flow regimes can be defined according to the sign of the pressure drop $\Delta\tilde{P}$ or, equivalently, to the sign of the hydraulic gradient $i=\frac{\Delta\tilde{P}}{\rho_w g H}$.

(i) *Stabilizing regime* ($i<0$). A downward water flow in the cell frame which exerts an over stress against y inside the porous medium.

(ii) *Destabilizing regime* ($i>0$). An upward water flow in the cell frame which tends to partially, or eventually totally, fluidize the granular bed.

The ultimate state of the destabilizing regime defines the fluidization threshold, when the overall drag force exerted on the whole medium by the water flow balances exactly the immersed weight of the grains. Higher water velocities yield a *fluidized regime*. The critical pressure drop for fluidization simply reads $\Delta\tilde{P}_c=(\rho-\rho_w)gH$, where ρ, the bulk density, is equal to $\rho=\Phi\rho_g+(1-\Phi)\rho_w$ with ρ_g the density of the grains and Φ the volume fraction of the medium. The corresponding *critical gradient* reads

$$i_c=\frac{\rho-\rho_w}{\rho_w}=\Phi\frac{(\rho_g-\rho_w)}{\rho_w}. \tag{3}$$

The different regimes, and especially the transition from static to fluidized medium, are clearly shown in Fig. 4 where the hydraulic gradient i is plotted as a function of the inner water velocity v for a granular bed constituted of glass beads ($d=1.0\pm0.1$ mm, $\rho_g=2.59$ g cm^{-3}), with an initial height $H=15.6$ cm and a static volume fraction $\Phi=0.600$. The water velocity within the granular layer is deduced from a floating indicator flowmeter measurement. The experimental fluidization onset corresponds to $i_c^{exp}\simeq0.89$, slightly smaller than the theoretical value $i_c\approx0.95$ deduced from Eq. (3). This might be due to geometrical effects at the corners of the cell where the water velocity is slightly higher than in the rest of the sample and induces locally immature fluidization little before the whole bed becomes fluidized.

In such a porous medium, the velocity is commonly given by Darcy's law [8]:

$$\underline{v}=-\frac{k}{\eta_w}(\text{grad}\,P-\rho_w\underline{g}), \tag{4}$$

where k is the permeability of the medium and η_w the viscosity of water ($\eta_w\simeq10^{-3}$ kg m^{-1} s^{-1}). In practice, this relation is valid as long as viscous forces remain predominant. This corresponds to Reynolds numbers based on average grain diameter d, $\text{Re}=\frac{\rho_w v d}{\eta_w}$, that do not exceed some value about 10 [8]. Above this limit, the flow is no more purely laminar and the following empirical relation, called Ergun's law, is often used [8]:

$$\frac{\Delta\tilde{P}}{H}=\frac{150\eta_w}{d^2}\frac{\Phi^2}{(1-\Phi)^3}v+\frac{1.75\rho_w}{d}\frac{\Phi}{(1-\Phi)^3}v^2. \tag{5}$$

In the first term, one recovers Darcy's relation with a specific expression of the permeability, $k_E=\frac{(1-\Phi)^3d^2}{150\Phi^2}$. The second term is purely empirical and accounts for inertial effects. In our experiments, this quadratic correction is negligible except for grains with diameter upper 1 mm for which Re can exceed 10. Such a case is presented in Fig. 4: while i remains smaller than i_c^{exp}, the experimental data are well approximated by Eq. (5). By fitting, a value $k_{exp}=(1.16\pm0.04)\times10^{-9}$ m^2 is obtained for the permeability, in very close agreement with the above expression proposed in the Ergun's law, $k_E=1.19\times10^{-9}$ m^2.

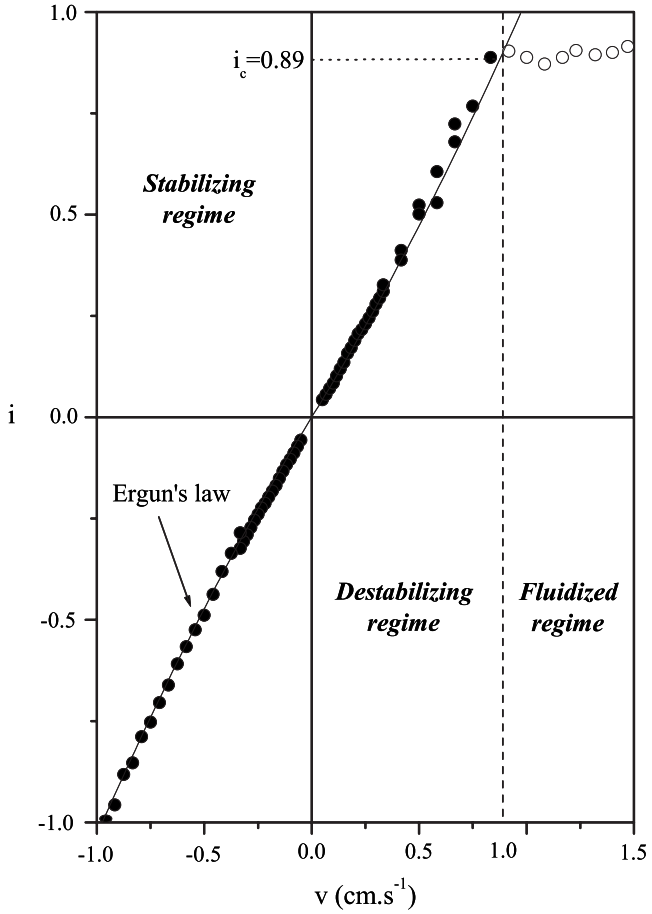

FIG. 4. Hydraulic gradient versus water velocity in a granular bed ($H=15.6$ cm and $\Phi=0.600$) constituted of glass beads ($d=1.0\pm0.1$ mm). The empirical Ergun's law defined in Eq. (5) is represented by the solid line.

III. THEORETICAL PREDICTION OF THE AVALANCHE ANGLE

The aim of this section is to account for the overall drag force induced by the water flow in the mechanical equilibrium of the medium and then, with an adapted criterion for destabilization, to evaluate theoretically the instability threshold, i.e., the avalanche angle. To do this, two alternative approaches can be used. First, the granular bed can be considered as a continuum medium and the stability is discussed in terms of stress equilibrium. Second, considering a sphere at the top surface of an assembly of equal spheres, it is possible to calculate the maximum inclination of the surface below which the local equilibrium of the upper sphere is

ensured. We will show in the following that both the continuum and the discrete approaches give exactly the same prediction.

A. Continuum medium approach

The two-dimensional stress equilibrium equation of the granular layer is

$$\mathrm{div}\ \underline{\underline{\sigma^g}} - \mathrm{grad}\ P + \rho \underline{g} = \underline{0}, \tag{6}$$

where $\underline{\underline{\sigma^g}}$ is the granular stress tensor, P the total water pressure, and ρ the bulk density.

By substituting Eq. (1) into Eq. (6), we obtain with the coordinate axes defined in Fig. 2,

$$\frac{\partial \sigma^g_{xx}}{\partial x} + \frac{\partial \sigma^g_{xy}}{\partial y} = -(\rho - \rho_w) g \sin\theta, \tag{7}$$

$$\frac{\partial \sigma^g_{xy}}{\partial x} + \frac{\partial \sigma^g_{yy}}{\partial y} = \frac{\partial \tilde{P}}{\partial y} + (\rho - \rho_w) g \cos\theta. \tag{8}$$

More details on this calculation of the granular stresses in a porous medium subjected to a nonhydrostatic gradient of fluid pressure can be found in [7,9,10] and references therein.

In the frame of an infinite slope hypothesis, the stress components are assumed to be independent of x. Assuming also that the medium is homogeneous, one obtains $\frac{\partial \tilde{P}}{\partial y} = -\frac{\Delta \tilde{P}}{H}$. Then, the set of equations (7) and (8) is simply solved and gives

$$\sigma^g_{xy} = (\rho - \rho_w) g \sin\theta (H - y), \tag{9}$$

$$\sigma^g_{yy} = -(\rho - \rho_w) g \left(\cos\theta - \frac{\Delta \tilde{P}}{\Delta \tilde{P}_c} \right) (H - y), \tag{10}$$

where $\Delta \tilde{P}_c$ is the critical pressure drop introduced previously in Sec. II.

Finally, the stability threshold can be determined by assuming a Mohr-Coulomb criterion for the stability condition of the granular stress,

$$|\sigma^g_{xy}| < \tan\varphi |\sigma^g_{yy}|, \tag{11}$$

where $\mu = \tan\varphi$ is an effective friction coefficient. Note that it is unclear if there is a real link between φ and the so-called *angle of internal friction* which is commonly used in soil mechanics but with quite higher stress conditions. As proved in [11], Eq. (11) is a necessary and sufficient condition of stability. After some algebra, the maximum angle of stability, i.e., the so-called avalanche angle θ_a, can be written as a function of the hydraulic gradient i and of the critical gradient i_c defined in Eq. (3),

$$\theta_a(i) = \varphi - \arcsin\left(\frac{i}{i_c} \sin\varphi \right). \tag{12}$$

B. Discrete approach

The same result can be obtained by an alternative approach based on the equilibrium of an individual grain situated at the upper layer of the granular medium as depicted in Fig. 5. For such a grain, the momentum equilibrium is more easily broken than the force equilibrium [5]. Let O be the center of the grain and P the pivot point around which the grain will first rotate. P is defined so as the resultant momentum of the contact forces around P is zero. The other forces to be considered in the momentum equation are the immersed weight of the grain $\underline{W}$, which is vertical, and the drag force $\underline{D}$ exerted by the flow on the grain, perpendicular in average to the free surface. Denoting by ψ the angle between $\underline{OP}$ and $-\underline{y}$, the unit inward normal to the free surface, one finds that the grain starts rolling as soon as the following condition is reached [5]:

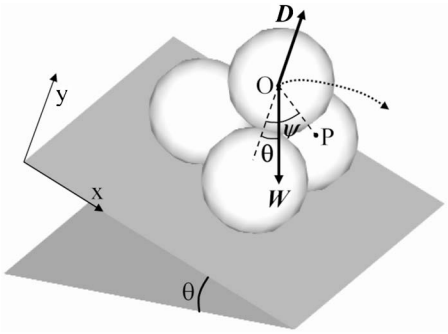

FIG. 5. Diagram for the calculation of the momentum equilibrium of a spherical grain at the upper surface of the granular bed. O is the center of the grain, P the pivot point, θ the inclination, and ψ the angle defining the geometrical trapping of the sphere. W is the vertical immersed weight and D the drag force exerted by the flow, perpendicular to the upper surface.

$$D \|\underline{OP}\| \sin(\psi) > W \|\underline{OP}\| \sin(\psi - \theta). \tag{13}$$

Equation (13) also reads

$$\frac{D}{W} > \cos\theta \left(1 - \frac{\tan\theta}{\tan\psi} \right). \tag{14}$$

As each grain in the upper layer has a particular geometrical configuration, Eq. (14) must be averaged over all these configurations. The notation $\langle\ \rangle$ is used for the corresponding average values. As the grains are all identical, W is constant and one obtains

$$\frac{\langle D \rangle}{W} > \cos\theta \left(1 - \frac{\tan\theta}{\tan\Psi} \right) = \frac{\sin(\Psi - \theta)}{\sin\Psi}, \tag{15}$$

where the angle Ψ is defined by

$$\frac{1}{\tan\Psi} = \left\langle \frac{1}{\tan\psi} \right\rangle. \tag{16}$$

For instance, to obtain an order of magnitude for Ψ, we can analyze the ideal case of a regular packing of spherical grains. The most favorable situation for a sphere to become destabilized is to roll over the valley constituted by two underlying grains, whereas in the most stable scenario the grain rolls over the summit of one of the underlying grains. By geometrical considerations one finds the two limiting values for $\tan\psi$, respectively $\tan\psi_m = \frac{\sqrt{2}}{4}$ and $\tan\psi_M = \frac{\sqrt{2}}{2}$ (see [5] for

details). In between these two limits, any intermediate situation is equiprobable. In the hydrostatic situation, Albert *et al.* have derived in [12] a general expression for ψ as a function of ϕ where ϕ denotes the angle between the steepest slope direction and the local orientation of the base spheres: $\psi(\phi)=\arctan[1/2\sqrt{2}\cos(\pi/3-\phi)]$ with $0<\phi<\pi/3$. Note that, for the two extreme cases where $\phi=0$ and $\phi=\pi/3$, we recover the values of $\tan\psi_M$ and $\tan\psi_m$ calculated above. As ϕ is randomly distributed at the upper surface of a pile, they have evaluated the mean maximum stability angle to $\langle\psi\rangle=(3/\pi)\int_0^{\pi/3}\psi(\phi)d\phi\simeq 23.4°$. Here, in presence of an additional drag force, we can use the same procedure to evaluate Ψ from Eq. (16),

$$\frac{1}{\tan\Psi}=\frac{3}{\pi}\int_0^{\pi/3}\frac{d\phi}{\tan\psi(\phi)}=\frac{3\sqrt{6}}{\pi}. \tag{17}$$

One obtains a slightly smaller value, $\Psi\simeq 23.1°$, quite reasonable compared to the experimental results obtained with almost monosize glass spheres and presented in Sec. IV.

The immersed weight of a grain reads $W=(\rho_g-\rho_w)g\omega_g$, where ω_g is the volume of the grain and ρ_g its density. The average drag force acting on a grain at the upper surface must be carefully evaluated. In [4], it is assumed that this force is weaker at the upper surface than inside the medium and a specific expression is proposed which appears to us rather questionable and unconfirmed. On the contrary, we assume here that, in average, the drag force exerted by the flow is the same on any grain of the medium, whatever its position in the bulk or at the upper surface. Then, the average drag force $\langle D\rangle$ is derived in the same way as in [3]. Let Ω be the volume of the whole granular layer and S its surface. As the medium is assumed to be homogeneous, the overall drag force F_D acting on Ω is simply given by the nonhydrostatic part of the total pressure force,

$$\underline{F_D}=\oint_S \tilde{P}\underline{dS}=\int_\Omega -\operatorname{grad}\tilde{P}d\Omega$$

$$=-\operatorname{grad}\tilde{P}\Omega=\frac{\Delta\tilde{P}}{H}\Omega\underline{y}=\rho_w g i\Omega\underline{y}. \tag{18}$$

The number of grains in the medium is $N=\Omega_g/\omega_g$, where Ω_g, the total volume occupied by the grains, is related to the solid volume fraction Φ by $\Omega_g=\Phi\Omega$. Then, according to Eq. (3), the average drag force per particle reads

$$\langle D\rangle=\frac{\|\underline{F_D}\|}{N}=\frac{\rho_w g i\omega_g}{\Phi}=\frac{i}{i_c}W. \tag{19}$$

Finally, Eq. (15) together with Eq. (19) gives exactly the same relation than Eq. (12) for the avalanche angle as a function of the hydraulic gradient, except that φ is replaced by Ψ. In fact, this is not so surprising since $\langle D\rangle$ is calculated by a mean field approximation which is equivalent to a continuum medium assumption. Note also that, although the parameters φ and Ψ have two different physical meanings, namely an effective friction coefficient and a mean geometrical stability angle, they both correspond to the avalanche angle measured in the classical hydrostatic situation where there is no water flow within the granular layer, $\varphi=\Psi=\theta_a(0)$. So a general expression for the angle of stability can be written as follows, without any adjustable parameter:

$$\theta_a(i)=\theta_a(0)-\arcsin\left(\frac{i}{i_c}\sin\theta_a(0)\right). \tag{20}$$

By comparison to the previous theoretical predictions for the avalanche angle, Eqs. (12) and (20) are identical, within the convention of sign for i, to the calculations proposed in [4] (continuum mode), in [5] (individual particle equilibrium), and in [6] (particle equilibrium at low Re). But the other expressions in [4] (single particle mode) and in [6] (continuum approach and particle equilibrium at high Reynolds numbers) differ notably from ours, which has the advantage to unify discrete and continuum approaches. We can also notice that, in the framework of sand erosion, the ratio $\frac{i}{i_c}$ can be interpreted as a Shields number Θ. Indeed, the dimensionless Shields number Θ is used to describe the erosion threshold and compares the immersed weight of a grain to the drag stress τ_f induced by the fluid flow: $\Theta=\frac{\tau_f}{(\rho_g-\rho_w)gd}$ (see [17] for instance). Here, from Eq. (19), we can derive $\tau_f=\frac{\rho_w g i d}{\Phi}$ and it directly follows that $\Theta=\frac{i}{i_c}$. Note that this result also means that, instead of the hydraulic gradient $i=\frac{\Delta\tilde{P}}{\rho_w g H}$ which is commonly used by hydrologists, a more appropriate choice for the nondimensional pressure drop in a granular soil would be $\frac{\Delta\tilde{P}}{(\rho-\rho_w)gH}$, which is directly equal to the Shields number Θ.

IV. EXPERIMENTAL RESULTS

A. Avalanche threshold

A large set of experimental data have been collected and confronted to the theoretical prediction. The measurements of the avalanche angle are performed as follows: once the cell has been closed with a given mass of grains inside it, a significant upward water flow is used to gently fluidize the granular medium. Afterwards, the flow is slowly decreased owing for a progressive settling down of the grains. This way, we obtain a fairly reproducible sample with a constant height H and with an almost flat upper surface. The height H is measured with a precision estimated to $\delta H=1$ mm. The corresponding values of the volume fraction Φ, obtained for the different granular samples, are reported in Table I with an uncertainty of measurement $\delta\Phi\leqslant 0.005$. These are intermediate values of the volume fraction, in between loose and dense packings. As could be expected, the volume fraction tends to increase when the polydispersity of the grains becomes larger in proportion to the mean diameter. Two last comments must be pointed out. First, since the different granular samples have experienced the same prefluidization procedure, they can be reasonably compared to each other. Second, the dynamics of immersed granular media very strongly depends on the bulk density and so it was imperative to control accurately the initial volume fraction of the samples so as to ensure the reproducibility of the results.

Starting from this reproducible initial configuration obtained with the prefluidization procedure, a water flow is applied within the granular layer and the pressure drop is

TABLE I. Characteristics of the granular materials studied in this paper, constituted either of glass beads (GB) or of natural sand (S). Corresponding volume fraction values obtained with the prefluidization protocol and practically reproducible for each material. The uncertainty of the volume fraction measurement is estimated to $\delta\Phi \leqslant 0.005$.

Granular material	Grains size (mm)	Grains density (g cm^{-3})	Volume fraction
GB	0.3–0.4	2.47	0.605
GB	0.4–0.6	2.50	0.606
GB	0.5–0.75	2.49	0.612
GB	1.0 ± 0.1	2.59	0.600
GB	1.6 ± 0.05	2.51	0.599
GB	1.97 ± 0.06	2.55	0.588
GB	2.95 ± 0.07	2.50	0.594
S	0.4–0.8	2.65	0.550

measured by a differential pressure sensor. Then, with this gradient kept constant, the cell is slowly rotated at constant rate until an avalanche triggers at the free surface. The corresponding inclination is the avalanche angle θ_a. Note that the granular sample is confined between the front and the back walls of the cell by a sufficiently large distance, namely 5 cm, to prevent any wall effect, even for the largest beads used here ($d \simeq 3$ mm) [13].

In a few number of experiments, an alternative protocol has been used: in the destabilizing regime ($i > 0$), the cell is first rotated to a given angle θ_a; then a slight upward flow is activated and progressively increased until initiation of the avalanche. The pressure drop is recorded just before the instability. Inversely, in the stabilizing regime ($i < 0$), to allow an important inclination of the cell (up to 90°), a high downward flow is first applied and then slowly decreased down to destabilization of the granular sample. We have checked that the two protocols give the same results within the error bars. As the first procedure is easier to implement, it has been systematically used in the following.

In Fig. 6, the avalanche angles measured for two granular samples constituted of glass beads ($d = 1.0 \pm 0.1$ mm) at a constant volume fraction ($\Phi = 0.600$) and with two different heights ($H = 12.0$ cm and $H = 18.4$ cm) are plotted as a function of the hydraulic gradient i. The experimental points collapse nicely on the theoretical curve without any adjustable parameter. Indeed, the two parameters in Eq. (20), namely the critical gradient i_c and the avalanche angle without water flow $\theta_a(0)$, are both known: the critical gradient is evaluated to $i_c \approx 0.95$ (see Sec. II) and $\theta_a(0)$ is directly measured equal to $\theta_a(0) = 27.5° \pm 0.5°$. For all the experiments on glass beads samples, with diameters ranging from 0.3 to 3 mm and volume fractions about 0.60, we have found almost the same value within the range $26° < \theta_a(0) < 32°$. Although slightly larger, these avalanche angles are comparable to those accurately measured in [14]. As already mentioned before, these experimental values are not too far from the theoretical estimate of Ψ calculated in Sec. III B ($\Psi \sim 23°$). By contrast, the value measured for the natural sand is significantly larger, around 45°. In Fig. 7, to compare each other

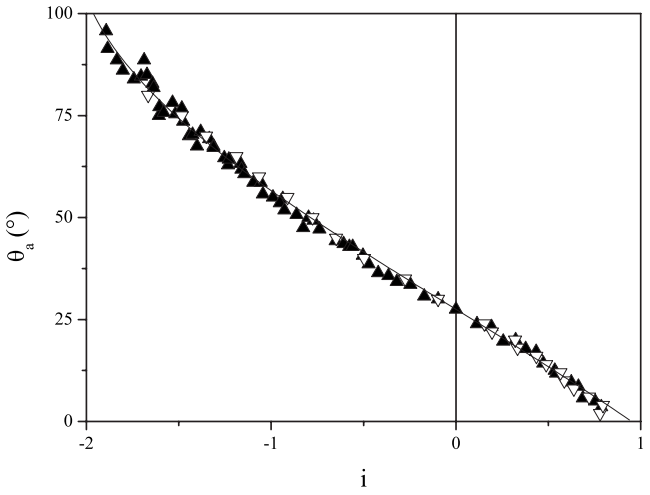

FIG. 6. Plot of the avalanche angle θ_a as a function of the hydraulic gradient i in two different samples constituted of the same glass beads ($d = 1.0 \pm 0.1$ mm) with two different heights: $H = 12.0$ cm, $\Phi = 0.600$ (▲) and $H = 18.4$ cm, $\Phi = 0.600$ (△). The solid line corresponds to the theoretical prediction given by Eq. (20) with $i_c = 0.95$ and $\theta_a(0) = 27.5°$. The size of the symbols indicates the error bars.

the measurements obtained with different values of $\theta_a(0)$ and i_c, all the data collected for many glass beads samples and for one natural sand sample are plotted in a diagram representing $\theta_a(i) - \theta_a(0)$ as a function of $\sin[\theta_a(0)] i/i_c$. This way,

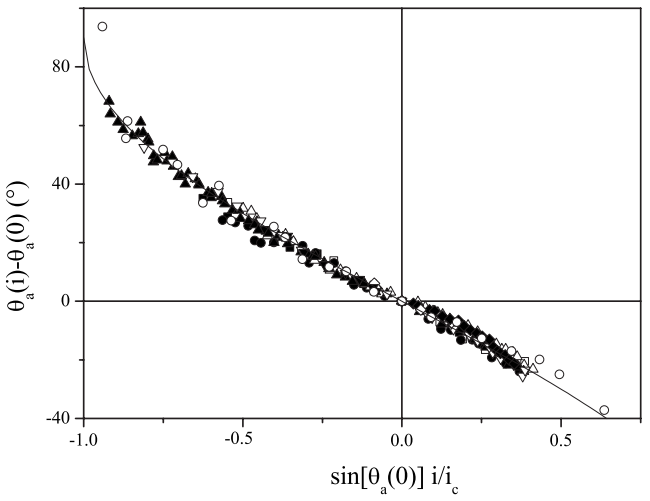

FIG. 7. Collapse of all the collected data by plotting $\theta_a(i) - \theta_a(0)$ as a function of $\sin[\theta_a(0)] i/i_c$. The solid line represents $f(x) = -\arcsin(x)$ and corresponds to the theoretical prediction. These data points have been obtained with several samples of glass beads (GB) and with one sample of sand (S): (GB) $0.3 < d < 0.4$ mm, $H = 10.7$ cm, $\Phi = 0.605$ (■); (GB) $0.4 < d < 0.6$ mm, $H = 16.5$ cm, $\Phi = 0.606$ (□); (GB) $0.5 < d < 0.75$ mm, $H = 16.4$ cm, $\Phi = 0.612$ (●); (GB) $d = 1.0 \pm 0.1$ mm, $H = 12.0$ cm, $\Phi = 0.600$ (▲); (GB) $d = 1.0 \pm 0.1$ mm, $H = 18.4$ cm, $\Phi = 0.600$ (▽); (GB) $d = 1.60 \pm 0.05$ mm, $H = 13.5$ cm, $\Phi = 0.599$ (△); (GB) $d = 1.97 \pm 0.06$ mm, $H = 13.4$ cm, $\Phi = 0.588$ (◆); (GB) $d = 2.95 \pm 0.07$ mm, $H = 13.4$ cm, $\Phi = 0.594$ (◇); (S) $0.4 < d < 0.8$ mm, $H = 15.3$ cm, $\Phi = 0.550$ (○).

all the points collapse almost perfectly, in very close agreement with the theoretical prediction, which is represented here by the curve $f(x)=-\arcsin(x)$.

Several observations can be made with regard to these results. First, we have obtained a very good agreement between the theoretical calculation and the experimental data, without any parameter adjustment as used in [5] or any change of the theoretical expression depending on the direction of the seepage flow as observed in [4]. Moreover, in comparison to these previous studies, much more materials have been tested here and a significantly larger range of avalanche angles is proposed. Second, a specific difficulty must be pointed out concerning the evaluation of the avalanche angle in the destabilizing regime. Indeed, as will be discussed later, the dynamics of the instability is rather progressive in this case and makes it hard to clearly detect the avalanche inset by direct observation, especially close to the fluidization threshold. Finally, the two extreme situations, namely over stabilized versus nearly fluidized medium, require some additional remarks. In the later case, as previously noticed in Sec. II, the experimental fluidization gradient is a bit smaller then the critical gradient i_c and, consequently, the data slightly departs from the theoretical prediction when i tends to i_c as can be seen in Fig. 6. In the opposite situation, for a granular medium stabilized by an intense inward water flow, very high values of the avalanche angles can be observed, up to more than 90° (see Figs. 6 and 7). According to the theoretical prediction, the maximum angle, equal to $\theta_a(0)+90°$, is obtained for $i=-i_c \sin[\theta_a(0)]$ and for $i<-i_c \sin[\theta_a(0)]$; the sample should remain stable whatever the inclination of the cell. This situation has been tested experimentally: a sand sample, with a high enough inward stabilizing flow, can be completely tilted, upside down. But this configuration is very sensitive to any moderate flow rate fluctuation or external perturbation.

B. Avalanche dynamics

Once the inclination of the granular sample has reached the stability threshold, the mechanical equilibrium of the medium is no more ensured and an avalanche triggers, leading to a transitory phase of grains motion in the upper part of the sample until total deposition of the mobile layer. When there is no water flow within the medium, it is well known that a subaqueous avalanche of large enough grains is almost similar to a dry one since the pore pressure, i.e., the nonhydrostatic pressure, remains negligible in the granular sample. For smaller grains, the permeability decreases over several orders of magnitude and a macroscopic deformation of the medium can possibly generate high pore pressures, susceptible to modify significantly the development of the instability [2]. Note that, according to its packing density, a granular medium must either dilate or compact when it starts to flow and the initial volume fraction is thus a rather critical parameter. At the present time, the influence of the interstitial fluid on the unsteady motion of a granular medium is still not clearly understood and this issue is accurately investigated (see, for instance, Refs. [15–17]).

In our study, because of the forced water flow within the sample, a pore pressure gradient is already present inside the medium before its destabilization and can influence the subsequent development of the avalanche. However, the coupling between the deformation of the granular medium and the inner water flow is not that simple and the present study does not aim to answer this complex issue. By now, only some obvious observations can be pointed out and reveal an avalanching dynamics qualitatively different in the stabilizing and in the destabilizing regime.

(a) In the stabilizing regime, very high inclines are achieved and, when the slope failure threshold is reached, a thin layer of grains starts flowing near the left lateral wall and runs downward over the upper surface. Then, in a very fast dynamics, the avalanche becomes deeper inside the sample in the upstream region, eroding extremely rapidly a large amount of grains which are subsequently deposited downstream, against the right lateral wall. The whole process is abrupt, nearly instantaneous, highly nonstationary, and mobilizes a great number of grains.

(b) In the destabilizing regime, the granular sample is contrarily only slightly tilted and the transition from a static pile to flowing grains appears to be very progressive: at first, the medium seems to slowly and gradually move as a whole before a moderate avalanche triggers at the upper surface so as to partially flatten the slope. The flowing layer remains limited to a small extent and the transition from a slow collective motion to a superficial flow becomes rather blurred, especially close to the fluidization inset. So, as already mentioned in Sec. IV A, it is quite hard to determine precisely the avalanche inset by a simple visual observation and an almost objective criterion was chosen for the data collected in Figs. 6 and 7: the instability threshold is reached as soon as the entire upper layer of the sample is flowing.

(c) By comparison, in the classical situation when there is no water flow within the granular bed, an intermediate dynamical behavior is observed: a tiny progressive deformation of the sample ultimately followed by a rather fast and massive destabilization.

These qualitative observations are only a preliminary analysis of the dynamical development of a gravitational instability in the situation of an inner water flow. This issue will be investigated more in depth, in a future work, by use of a fast camera since the duration of these avalanches are too small for standard images recording rates. In particular, a systematic study will be carried out to clarify the relative influences of the hydraulic gradient, of the grains size, and of the volume fraction which is believed to be quite substantial, as already mentioned in Sec. IV A.

C. Postavalanche interface

The last point discussed in this section concerns the static shape of the free surface following avalanches. For the purely hydrostatic situation, it is well known that the upper surface of the granular bed is linear with an inclination slightly smaller than the avalanche angle θ_a: the so-called *repose angle* θ_r. For the glass beads used in this study, in rather closed packed configurations, θ_r remains in the range $20° < \theta_r < 23°$. That is to say $\Delta\theta \sim 6° - 9°$ below the corresponding values of the avalanche angle. Note that these val-

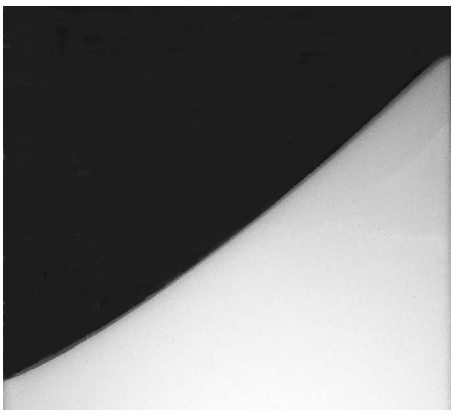

FIG. 8. Typical picture of the free surface following an avalanche in the stabilizing regime ($i<0$).

ues are more or less comparable to the ones measured in [14], except for $\Delta\theta$ which is appreciably larger, maybe because of the different experimental configurations (rectangular cell versus rotating drum) and bed's initial conditions (prefluidized sample versus previous avalanche deposit). On the other hand, when water flows within the grains layer, we can observe that the interface of the granular deposit is no more linear and becomes progressively curved. In the destabilizing regime, the avalanche angles are quite small and this effect is scarcely visible. By contrast, in the stabilizing regime with higher values of θ_a, the upper surface departs notably from a linear shape as can be seen in Fig. 8.

This nonlinear shape of the sample free surface can be simply understood: after deposition of the avalanche, the granular bed does not have a constant height anymore and the streamlines of the inner water flow are thus significantly modified. The nonhydrostatic pressure gradient is consequently no more constant in the sample: it increases where the bed becomes thinner, i.e., upstream the avalanche direction, and decreases downstream. In the following, a model is developed to account for this effect.

1. Model

The diagrams in Fig. 9 represent a granular sample before and after an avalanche. Before the instability triggers, the sample has a constant thickness H and undergoes a uniform hydraulic gradient i_0. After the avalanche, the sample height is no more constant and, consequently, so is the superficial hydraulic gradient. As shown in Fig. 9, the following local quantities can be defined at an abscissa x: height $h(x)$, hydraulic gradient $i(x)$ (locally perpendicular to the interface), repose angle $\theta_r(x)$, and local slope $\beta(x)$. Note that $\beta(x)$ is related to the height by

$$\frac{dh}{dx} = \tan \beta(x). \tag{21}$$

It has been obtained theoretically in Sec. III and confirmed experimentally in Sec. IV that the avalanche threshold is related to the hydraulic gradient i_0 by $\theta_a(i_0)=\theta_a(0) - \arcsin[i_0/i_c \sin \theta_a(0)]$. Let us assume that, no more at a macroscopic but also at an intermediate scale, an analog relation holds between the local repose angle and the superficial hydraulic gradient,

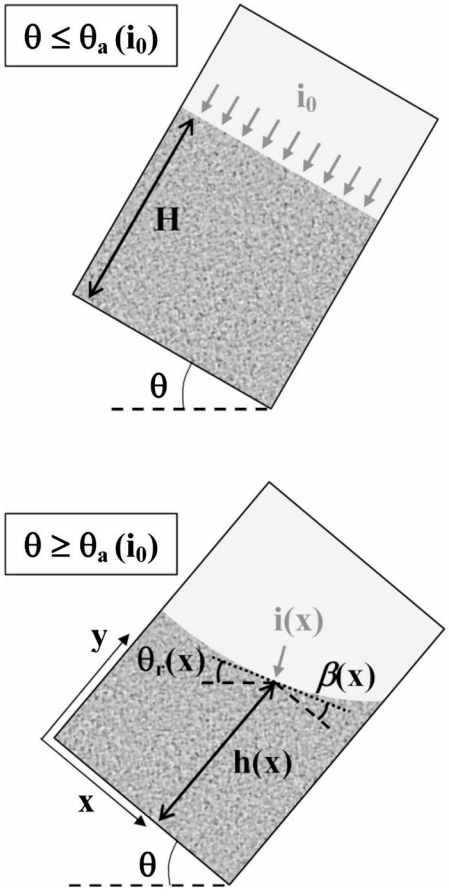

FIG. 9. Diagrams of the experimental cell for two successive inclinations, below and above the avalanche threshold $\theta_a(i_0)$. Initially the granular sample has a constant thickness H and undergoes a uniform hydraulic gradient i_0 (here in the stabilizing regime with $i_0<0$). In the postavalanche situation, at an abscissa x, the following local quantities are introduced: height $h(x)$, superficial hydraulic gradient $i(x)$ (perpendicular to the interface), repose angle $\theta_r(x)$, and local slope $\beta(x)$ [defined by $dh/dx=\tan \beta(x)$].

$$\theta_r(i(x)) = \theta_r(0) - \arcsin\left[\frac{i(x)}{i_c} \sin \theta_r(0)\right]. \tag{22}$$

As can be seen on the postavalanche diagram in Fig. 9, the local slope $\beta(x)$ is related to the local repose angle by

$$\beta(x) = \theta - \theta_r[i(x)], \tag{23}$$

where θ is the inclination of the cell. This gives the following expression for $\beta(x)$:

$$\beta(x) = \theta - \theta_r(0) + \arcsin\left[\frac{i(x)}{i_c} \sin \theta_r(0)\right]. \tag{24}$$

The next step consists in evaluating the local hydraulic gradient $i(x)$ at the upper surface. To do this, the nonhydrostatic pressure field $\tilde{P}(x,y)$ must be calculated in a porous layer with a variable thickness $h(x)$. Assuming first that the water velocity $\underline{v}$ is given by Darcy's law in Eq. (4) and

second that water is incompressible, div $\underline{v}=0$, the Laplace equation $\Delta\tilde{P}=0$ holds and must be solved. An approximate analytical solution can be derived by a two-stage procedure. The calculation is first carried out for a linear upper surface of the porous medium and without any lateral boundary conditions. Then, the previous solution is generalized to a slowly variable profile $h(x)$ but, here again, the influence of the lateral walls is neglected. The detailed calculation is presented in Appendix A and gives in the end the following approximate expression for the local superficial hydraulic gradient $i(x)$:

$$i(x) = i_0 \frac{\tan\beta(x)}{\beta(x)} \frac{H}{h(x)}. \quad (25)$$

2. Solution and validation

To calculate the free surface profile of the postavalanche deposit, we must solve equations (21), (24), and (25) that relate locally, at the upper surface, the slope $\beta(x)$, the height $h(x)$, and the hydraulic gradient $i(x)$.

A direct numerical integration is quite simple and the corresponding profiles can be confronted to several experimental data measured for a granular sample subjected to controlled inner water flows. The experimental data are obtained after image processing of high resolution pictures (2048 $\times$1536 pixels) similar to the one presented in Fig. 8. These pictures can be recorded either in the vicinity of the instability angle, just at the end of a massive avalanche, or for higher inclines, giving rise to slight subsequent superficial flows either intermittent or continuous according to the driving rotation rate of the cell. A comparison between theoretical and experimental profiles is presented in Fig. 10 for a glass beads sample ($0.3<d<0.4$ mm, $\Phi=0.605$, and $H=10.7$ cm) in the stabilizing regime ($i_0=-0.45$). An overall agreement is obtained, except in the upper part of the first profile at inclination $\theta=49.1°$. In this specific case, just after the instability threshold, an almost instantaneous avalanche first triggers, followed by a more moderate superficial flow which ensures the equilibration between the local slope and the pressure drop as postulated in Eq. (22). If, as observed here, this flow does not reach all the extent of the granular sample, the upper zone remains out of equilibrium in terms of local repose angle versus hydraulic gradient.

Concurrently to the direct numerical integration, an approximate solution can also be derived providing that the local hydraulic gradient $i(x)$ remains close enough to i_0, the constant hydraulic gradient before avalanche. More precisely, if $|i(x)-i_0| \ll i_c$, the set of equations (21), (24), and (25) can be linearized and, after Taylor expansions (see Appendix B for details), the following nonlinear first order differential equation is obtained:

$$\frac{dh}{dx} = \tan\beta^* \left(1 + \frac{h^*}{h(x)}\right), \quad (26)$$

where two parameters have been introduced. The first one, $\tan\beta^*$, reads, as a function of $\beta_0=\theta-\theta_r(i_0)$,

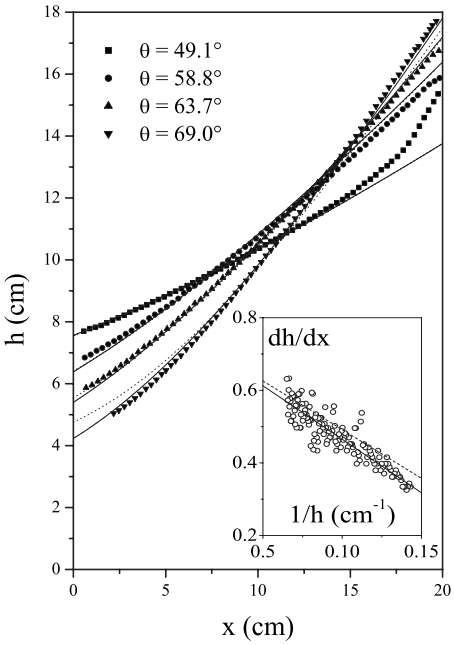

FIG. 10. Theoretical and experimental profiles obtained with an initial sample ($H=10.7$ cm, $\Phi=0.605$) constituted of glass beads, in the stabilizing regime ($i_0=-0.45$), for the following successive inclinations: $\theta=49.1°$, 58.8°, 63.7°, and 69.0°. The solid lines correspond to the direct numerical integrations and the dotted lines to the approximate solutions in Eq. (29). Inset: local slope evaluated from the experimental profile at $\theta=58.8°$ and compared to the prediction of Eq. (26) where the parameter h^* is either fixed (dotted line) or free (solid line).

$$\tan\beta^* = \tan\beta_0 - \frac{i_0 \sin\theta_r(0)}{i_c \cos^2\beta_0 \sqrt{1-[i_0/i_c \sin\theta_r(0)]^2}}. \quad (27)$$

The second parameter h^*, homogeneous to a height and negative (respectively, positive) in the stabilizing (respectively, destabilizing) regime, is defined by

$$h^* = H \frac{i_0 \tan\beta_0 \sin\theta_r(0)}{i_c \beta_0 \cos^2\beta_0 \tan\beta^* \sqrt{1-[i_0/i_c \sin\theta_r(0)]^2}}. \quad (28)$$

Finally, Eq. (26) can be integrated and gives the following implicit expression for the local height $h(x)$,

$$h(x) = H + \tan\beta^*(x-x_H) + h^* \ln\left(\frac{h(x)+h^*}{H+h^*}\right), \quad (29)$$

where x_H is the only unknown parameter of the model and corresponds to the position where the local height is equal to H, the initial thickness of the sample.

As can be seen in Fig. 10, there is only a slight deviation between the approximate solution and the direct numerical integration even when Eq. (29) is used out of the domain of validity of the Taylor expansions, i.e., when $|i(x)-i_0| \geqslant i_c$. The overall agreement with the experimental data is here again quite satisfactory. However, it should be noticed that in several cases, the accuracy of the theoretical profiles is not that good. We believe that this is due to the sensitivity in the evaluation of h^* and, in a smaller extent, of $\tan\beta^*$, to some

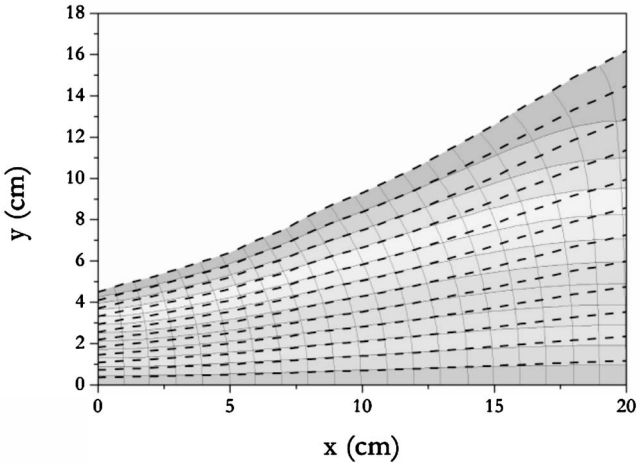

FIG. 11. Comparison between the exact isobaric lines (grayscale contours) and the approximate analytical expression (dashed lines) $y_\lambda(x)$ with $\lambda=0,0.1,\ldots,0.9,1$. The bed profile $h(x)$ has been measured for an initial sample ($H=16.5$ cm, $\Phi=0.606$) constituted of glass beads ($0.4<d<0.6$ mm) with $i_0=-0.34$ and $\theta=63.1°$.

slight variations of the different experimental control parameters, namely H, i_0, $\theta_r(0)$, and θ. The main sources of deviation can be identified: the unavoidable uncertainty of measurement, the statistical evaluation of $\theta_r(0)$, and, the last but not the least, the difference between the effective inclination of the cell at which the picture is taken and the *equilibrated* inclination, i.e., the angle at which the last surface avalanching flow has stopped. For these reasons, a bias can be observed between the expected values of $\tan\beta^*$ and h^* and the ones obtained by a fitting procedure when either both $\tan\beta^*$ and h^*, or only h^*, are set as free parameters (see for instance the inset in Fig. 10). This deviation remains moderate for $\tan\beta^*$ but can be more important for h^* whose dependence with β_0 in Eq. (28) is rather complex and, in particular, nonmonotonic.

3. Validity of the nonhydrostatic pressure field approximation

Since no lateral boundary conditions are considered in the calculation of Appendix A, the approximate solution of the nonhydrostatic pressure field given in Eq. (A6) is only acceptable far enough from the walls. Nevertheless its validity in all the granular layer can be checked *a posteriori*. Indeed, by use of a commercial software dedicated to groundwater flow analysis, the nonhydrostatic pressure field $\tilde{P}$ can be evaluated numerically. Then, this exact solution is compared to our approximate theoretical expression in Eq. (A6). The comparison is presented in Fig. 11 where several exact isobaric lines of pressure $\tilde{P}=\tilde{P}_1+\lambda(\tilde{P}_2-\tilde{P}_1)$, with $0<\lambda<1$, are plotted together with the approximated expression deduced from the model, namely,

$$y_\lambda(x)=h(x)\left(\frac{dh}{dx}\right)^{-1}\tan\left[\lambda\arctan\left(\frac{dh}{dx}\right)\right], \qquad (30)$$

where the local slope $\frac{dh}{dx}$ is given by Eq. (26).

As can be seen in Fig. 11, the approximate analytical expression deviates significantly from the exact solution close to the wall, especially in the right part of the sample. However, the overall agreement remains acceptable and, mentioning the accuracy the model, expressions (A6) and (25) appear as realistic approximations of the nonhydrostatic pressure field.

V. SUMMARY AND PERSPECTIVES

The gravitational instability of a granular material under a stationary inner water flow was investigated both experimentally and theoretically. The angle threshold at which an avalanche triggers was measured as a function of the hydraulic gradient i, the nondimensional pressure drop, for a natural sand sample and for several glass beads samples with different heights or particles sizes distributions. The experimental data are in very good agreement with a theoretical prediction derived concurrently by two alternative approaches: continuum medium theory and local equilibrium of discrete spheres.

In the vicinity of the avalanche threshold, the dynamical development of the instability reveals noticeable differences according to the water flow regime. In the stabilizing regime, with an inward water flow, the granular sample remains static, even for high inclinations, and, once the threshold is reached, a fast and massive avalanche triggers, mobilizing a large amount of grains. In the destabilizing regime, for a sample partially fluidized by the water flow, the destabilization is continuous and progressive until a quite moderate avalanche slightly flattens the free surface. By comparison, the more classical purely hydrostatic situation has an intermediate behavior with a slightly progressive motion of the whole granular sample until a rather large avalanche triggers. A further study will be dedicated to this dynamical behavior around the avalanche threshold. The influences of the water flow and of the bed characteristics (volume fraction, mean grains size, permeability) will be specifically analyzed.

Finally, in the two water flow regimes, the static shape of the granular sample following the first avalanche has no more a constant slope as in the usual case with no water flow. Indeed, the upper free surface departs significantly from a simple linear interface at the repose angle, especially in the stabilizing regime where high inclinations are reached. Assuming a local constitutive relation between the repose angle and the hydraulic gradient, and deriving an approximate expression of the nonhydrostatic pressure field, a numerical solution as well as an analytical implicit expression can be predicted for the sample profile in very good agreement with the measurements. The validity of the model is satisfactory confronted to numerical and approximated analytical solutions of the inner water flow.

ACKNOWLEDGMENTS

We are grateful to Olivier Pouliquen for fruitful discussions and for a careful reading of the manuscript. The authors acknowledge financial support from the French National Research Agency (ANR-PIGE).

APPENDIX A: APPROXIMATE LAPLACE EQUATION SOLUTION

A simplified analytical solution of the Laplace equation $\Delta\tilde{P}=0$ in a two-dimensional (2D) porous layer with a variable thickness $h(x)$ is proposed in the following. The situation is depicted in the bottom diagram of Fig. 9. No boundary conditions are imposed at the two lateral walls so that the subsequent solution will be valid only in the center part of the medium, far enough from the walls. The boundary conditions at the bottom and at the top of the medium are

$$\tilde{P}(x,0)=\tilde{P}_- \quad \text{and} \quad \tilde{P}[x,h(x)]=\tilde{P}_+. \tag{A1}$$

To solve the Laplace equation, we use the following change of variables

$$\tilde{P}(x,y)=G(x)F\left(u=\frac{y}{h(x)}\right). \tag{A2}$$

According to the boundary conditions in Eq. (A1), the function $G(x)$ is simply a constant which can be taken equal to 1 and, consequently, the function $F(u)$ satisfies $F(0)=\tilde{P}_-$ and $F(1)=\tilde{P}_+$. Then the Laplace equation reads

$$\Delta\tilde{P}=0=\left(2u\frac{h'^2}{h^2}-u\frac{h''}{h}\right)F'(u)+\frac{1+u^2h'^2}{h^2}F''(u). \tag{A3}$$

It follows

$$\frac{F''(u)}{F'(u)}=\frac{uhh''-2uh'^2}{1+u^2h'^2}, \tag{A4}$$

which can be integrated to give

$$F'(u)=A(x)(1+u^2h'^2)^{-1+(hh''/2h'^2)}, \tag{A5}$$

where $A(x)$ is a function to be determined by the boundary conditions. Equation (A5) can be integrated analytically if $h''=0$, that is to say for a linear profile given by $\frac{dh}{dx}=\tan\beta$. The subsequent expression reads

$$\tilde{P}(x,y)=\tilde{P}_-+\frac{(\tilde{P}_+-\tilde{P}_-)}{\beta}\arctan\left(\tan\beta\frac{y}{h(x)}\right). \tag{A6}$$

We can now evaluate at an abscissa x the superficial hydraulic gradient $\underline{i}(x)=i(x)\underline{n}(x)$, where $\underline{n}(x)$ is the normal unit vector at the upper free surface. From Eq. (2), one obtains

$$i(x)=\frac{\tan\beta}{\beta}\frac{(\tilde{P}_+-\tilde{P}_-)}{\rho_w g h(x)}=i_0\frac{\tan\beta}{\beta}\frac{H}{h(x)}. \tag{A7}$$

In this expression, we have introduced the hydraulic gradient $i_0=-\frac{\Delta\tilde{P}}{\rho_w g H}$ which corresponds to the uniform hydraulic gradient induced in a medium with a constant height H by the same difference of pressures $\Delta\tilde{P}=\tilde{P}_--\tilde{P}_+$ between the lower surface $(\tilde{P}_-)$ and the upper surface $(\tilde{P}_+)$. This corresponds to the reference situation below the avalanche threshold as depicted in Fig. 9.

Starting from this expression, we can investigate the case of a slightly variable height by assuming that the previous solution can be used locally: the constant slope $\tan\beta$ is then simply replaced by the local slope $\frac{dh}{dx}=\tan\beta(x)$. It follows

$$i(x)=i_0\frac{\tan\beta(x)}{\beta(x)}\frac{H}{h(x)}. \tag{A8}$$

APPENDIX B: LINEARIZED SOLUTION FOR THE POSTAVALANCHE PROFILE

Providing that $i(x)$ remains close to i_0 and, more precisely, that $|i(x)-i_0|\ll i_c$, we can linearize around i_0 the different equations of the model derived in Sec. IV C 1.

A first Taylor expansion of Eq. (22) gives

$$\theta_r[i(x)]\approx\theta_r(i_0)-\frac{[i(x)-i_0]\sin\theta_r(0)}{i_c\sqrt{1-[i_0/i_c\sin\theta_r(0)]^2}} \tag{B1}$$

with $\theta_r(i_0)$ given by

$$\theta_r(i_0)=\theta_r(0)-\arcsin\left(\frac{i_0}{i_c}\sin\theta_r(0)\right). \tag{B2}$$

It follows

$$\beta(x)\approx\beta_0+\Gamma[i(x)-i_0], \tag{B3}$$

with $\beta_0=\theta-\theta_r(i_0)$ and where, for convenience, Γ is defined in the following by

$$\Gamma=\frac{\sin\theta_r(0)}{i_c\sqrt{1-[i_0/i_c\sin\theta_r(0)]^2}}. \tag{B4}$$

Then, one obtains by Taylor expansion of Eq. (21),

$$\tan\beta(x)\approx\tan\beta_0+\frac{\Gamma[i(x)-i_0]}{\cos\beta_0^2}. \tag{B5}$$

From Eq. (24), the linearized hydraulic gradient $i(x)$ reads simply

$$i(x)\approx i_0\frac{\tan\beta_0}{\beta_0}\frac{H}{h(x)}. \tag{B6}$$

Equations (B5) and (B6) together with the definition of the local slope gives

$$\frac{dh}{dx}\approx\tan\beta_0-\frac{\Gamma i_0}{\cos^2\beta_0}+\frac{\Gamma i_0\tan\beta_0 H}{\beta_0\cos^2\beta_0 h(x)}, \tag{B7}$$

which can be written

$$\frac{dh}{dx}=\tan\beta^*\left(1+\frac{h^*}{h(x)}\right), \tag{B8}$$

where $\tan\beta^*$, a characteristic slope, and h^*, homogeneous to a height, are introduced as

$$\tan\beta^*=\tan\beta_0-\frac{\Gamma i_0}{\cos^2\beta_0} \tag{B9}$$

and

$$h^*=H\frac{\Gamma i_0\tan\beta_0}{\beta_0\cos^2\beta_0\tan\beta^*}. \tag{B10}$$

[1] M. A. Hampton, H. J. Lee, and J. Locat, Rev. Geophys. **34**, 33 (1996).
[2] R. M. Iverson, Rev. Geophys. **35**, 245 (1997).
[3] I. Vardoulakis, Geotechnique **54**, 117 (2004).
[4] C. van Rhee and A. Bezuijen, J. Geotech. Engrg. **118**, 1236 (1992).
[5] Y. Lu, Y. M. Chiew, and N. S. Cheng, in *Thirtieth IAHR Congress Proceedings, Thessaloniki (2003)*, edited by J. Ganoulis and P. Prinos (Aristoteleio Panepistimio Tessalonikis, Greece, 2003), pp. 549–556.
[6] I. Eames and M. A. Gilbertson, J. Fluid Mech. **424**, 169 (2000).
[7] R. P. Delinger and R. M. Iverson, Mar. Geotech. **9**, 299 (1990).
[8] J. Bear, *Dynamics of Fluids in Porous Media* (Elsevier, New York, 1972).
[9] R. Mourgues and P. R. Cobbold, Tectonophysics **376**, 75 (2003).
[10] R. M. Iverson and M. E. Reid, Water Resour. Res. **28**, 925 (1992).
[11] P. de Buhan and L. Dormieux, J. Geotech. Engrg. **119**, 2004 (1993).
[12] R. Albert, I. Albert, D. Hornbaker, P. Schiffer, and A.-L. Barabasi, Phys. Rev. E **56**, R6271 (1997).
[13] S. Courrech du Pont, P. Gondret, B. Perrin, and M. Rabaud, Europhys. Lett. **61**, 492 (2003).
[14] S. Courrech du Pont, P. Gondret, B. Perrin, and M. Rabaud, Phys. Rev. Lett. **90**, 044301 (2003).
[15] D. Doppler, P. Gondret, T. Loiseleux, S. Meyer, and M. Rabaud, J. Fluid Mech. **577**, 161 (2007).
[16] C. Cassar, M. Nicolas, and O. Pouliquen, Phys. Fluids **17**, 103301 (2005).
[17] T. Loiseleux, P. Gondret, M. Rabaud, and D. Doppler, Phys. Fluids **17**, 103304 (2005).